PRNet: Self-Supervised Learning for Partial-to-Partial Registration

Yue Wang
Massachusetts Institute of Technology
yuewangx@mit.edu

Justin Solomon
Massachusetts Institute of Technology
jsolomon@mit.edu

Abstract

We present a simple, flexible, and general framework titled Partial Registration Network (PRNet), for partial-to-partial point cloud registration. Inspired by recently-proposed learning-based methods for registration, we use deep networks to tackle non-convexity of the alignment and partial correspondence problems. While previous learning-based methods assume the entire shape is visible, PRNet is suitable for partial-to-partial registration, outperforming PointNetLK, DCP, and non-learning methods on synthetic data. PRNet is self-supervised, jointly learning an appropriate geometric representation, a keypoint detector that finds points in common between partial views, and keypoint-to-keypoint correspondences. We show PRNet predicts keypoints and correspondences consistently across views and objects. Furthermore, the learned representation is transferable to classification.

1 Introduction

Registration is the problem of predicting a rigid motion aligning one point cloud to another. Algorithms for this task have steadily improved, using machinery from vision, graphics, and optimization. These methods, however, are usually orders of magnitude slower than "vanilla" Iterative Closest Point (ICP), and some have hyperparameters that must be tuned case-by-case. The trade-off between efficiency and effectiveness is steep, reducing generalizability and/or practicality.

Recently, PointNetLK [1] and Deep Closest Point (DCP) [2] show that learning-based registration can be faster and more robust than classical methods, even when trained on different datasets. These methods, however, cannot handle partial-to-partial registration, and their one-shot constructions preclude refinement of the predicted alignment.

We introduce the Partial Registration Network (PRNet), a sequential decision-making framework designed to solve a broad class of registration problems. Like ICP, our method is designed to be applied *iteratively*, enabling coarse-to-fine refinement of an initial registration estimate. A critical new component of our framework is a keypoint detection sub-module, which identifies points that match in the input point clouds based on co-contextual information. Partial-to-partial point cloud registration then boils down to detecting keypoints the two point clouds have in common, matching these keypoints to one another, and solving the Procrustes problem.

Since PRNet is designed to be applied iteratively, we use Gumbel–Softmax [3] with a straight-through gradient estimator to sample keypoint correspondences. This new architecture and learning procedure modulates the sharpness of the matching; distant point clouds given to PRNet can be coarsely matched using a diffuse (fuzzy) matching, while the final refinement iterations prefer sharper maps. Rather than introducing another hyperparameter, PRNet uses a sub-network to predict the temperature [4] of the Gumbel–Softmax correspondence, which can be cast as a simplified version of the actor-critic method. That is, PRNet *learns* to modulate the level of map sharpness each time it is applied.

We train and test PRNet on ModelNet40 and on real data. We visualize the keypoints and correspondences for shapes from the same or different categories. We transfer the learned representations to shape classification using a linear SVM, achieving comparable performance to state-of-the-art supervised methods on ModelNet40.

Contributions. We summarize our key contributions as follows:

- We present the *Partial Registration Network* (PRNet), which enables partial-to-partial point cloud registration using deep networks with state-of-the-art performance.
- We use Gumbel–Softmax with straight-through gradient estimation to obtain a sharp and near-differentiable mapping function.
- We design an *actor-critic closest point* module to modulate the sharpness of the correspondence using an action network and a value network. This module predicts more accurate rigid transformations than differentiable soft correspondence methods with fixed parameters.
- We show registration is a useful proxy task to learn representations for 3D shapes. Our representations can be transferred to other tasks, including keypoint detection, correspondence prediction, and shape classification.
- We release our code to facilitate reproducibility and future research. [1]

2   Related Work

Rigid Registration. ICP [5] and variants [6, 7, 8, 9] have been widely used for registration. Recently, probabilistic models [10, 11, 12] have been proposed to handle uncertainty and partiality. Another trend is to improve the optimization: [13] applies Levenberg—Marquardt to the ICP objective, while global methods seek a solution using branch-and-bound [14], Riemannian optimization [15], convex relaxation [16], mixed-integer programming [17], and semidefinite programming [18].

Learning on Point Clouds and 3D Shapes. Deep Sets [19] and PointNet [20] pioneered deep learning on point sets, a challenge problem in learning and vision. These methods take coordinates as input, embed them to high-dimensional space using shared multilayer perceptrons (MLPs), and use a symmetric function (e.g., $\max$ or $\sum$) to aggregate features. Follow-up works incorporate local information, including PointNet++ [21], DGCNN [22], PointCNN [23], and PCNN [24]. Another branch of 3D learning designs convolution-like operations for shapes or applies graph convolutional networks (GCNs) [25, 26] to triangle meshes [27, 28], exemplifying architectures on non-Euclidean data termed *geometric deep learning* [29]. Other works, including SPLATNet [30], SplineCNN [31], KPConv [32], and GWCNN [33], transform 3D shapes to regular grids for feature learning.

Keypoints and Correspondence. Correspondence and registration are dual tasks. Correspondence is the approach while registration is the output, or vice versa. Countless efforts tackle the correspondence problem, either at the point-to-point or part-to-part level. Due to the $O(n^2)$ complexity of point-to-point correspondence matrices and $O(n!)$ possible permutations, most methods (e.g., [34, 35, 36, 37, 38, 39, 40, 41]) compute a sparse set of correspondences and extend them to dense maps, often with bijectivity as an assumption or regularizer. Other efforts use more exotic representations of correspondences. For example, functional maps [42] generalize to mappings between functions on shapes rather than points on shapes, expressing a map as a linear operator in the Laplace–Beltrami eigenbasis. Mathematical methods like functional maps can be made 'deep' using priors learned from data: Deep functional maps [43, 44] learn descriptors rather than designing them by hand.

For partial-to-partial registration, we cannot compute bijective correspondences, invalidating many past representations. Instead, keypoint detection is more secure. To extract a sparser representation, KeyPointNet [45] uses registration and multiview consistency as supervision to learn a keypoint detector on 2D images; our method performs keypoint detection on point clouds. In contrast to our model, which learns correspondences from registration, [46] uses correspondence prediction as the training objective to learn how to segment parts. In particular, it utilizes PointNet++ [21] to product point-wise features, generates matching using a correspondence proposal module, and finally trains the pipeline with ground-truth correspondences.

Self-supervised Learning. Humans learn knowledge not only from teachers but also by predicting and reasoning about unlabeled information. Inspired by this observation, self-supervised learning

---

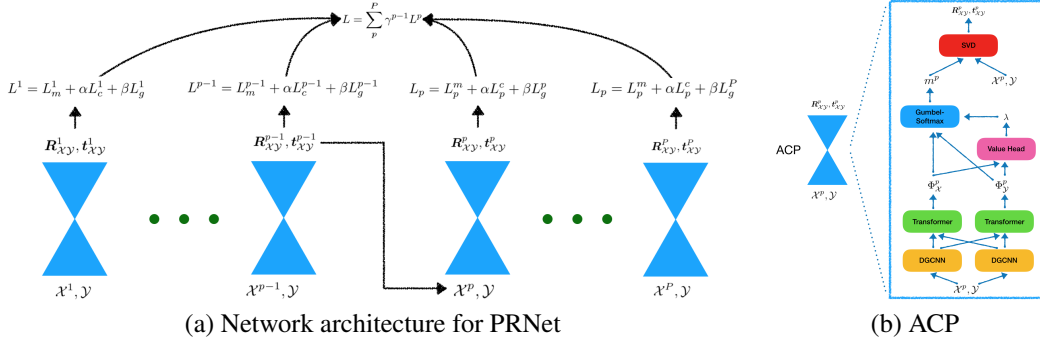(a) Network architecture for PRNet   (b) ACP

Figure 1: Network architecture for PRNet and ACP.

usually involves predicting part of an input from another part [47, 48], solving one task using features learned from another task [45] and/or enforcing consistency from different views/modalities [49, 50]. Self-supervised pretraining is an effective way to transfer knowledge learned from massive unlabeled data to tasks where labeled data is limited. For example, BERT [51] surpasses state-of-the-art in natural language processing by learning from contextual information. ImageNet Pretrain [52] commonly provides initialization for vision tasks. Video-audio joint analysis [53, 54, 55] utilizes modality consistency to learn representations. Our method is also self-supervised, in the sense that no labeled data is needed.

Actor–Critic Methods. Many recent works can be counted as actor–critic methods, including deep reinforcement learning [56], generative modeling [57], and sequence generation [58]. These methods generally involve two functions: taking actions and estimating values. The predicted values can be used to improve the actions while the values are collected when the models interact with environment. PRNet uses a sub-module (value head) to predict the level of granularity at which we should map two shapes. The value adjusts the temperature of Gumbel–Softmax in the action head.

3 Method

We establish preliminaries about the rigid alignment problem and related algorithms in §3.1; then, we present PRNet in §3.2. For ease of comparison to previous work, we use the same notation as [2].

3.1 Preliminaries: Registration, ICP, and DCP

Consider two point clouds $\mathcal{X} = \{\boldsymbol{x}_1, \ldots, \boldsymbol{x}_i, \ldots, \boldsymbol{x}_N\} \subset \mathbb{R}^3$ and $\mathcal{Y} = \{\boldsymbol{y}_1, \ldots, \boldsymbol{y}_j, \ldots, \boldsymbol{y}_M\} \subset \mathbb{R}^3$. The basic task in rigid registration is to find a rotation $\boldsymbol{R}_{\mathcal{XY}}$ and translation $\boldsymbol{t}_{\mathcal{XY}}$ that rigidly align $\mathcal{X}$ to $\mathcal{Y}$. When $M = N$, ICP and its peers approach this task by minimizing the objective function

$$E(\boldsymbol{R}_{\mathcal{XY}}, \boldsymbol{t}_{\mathcal{XY}}, m) = \frac{1}{N} \sum_{i=1}^{N} \|\boldsymbol{R}_{\mathcal{XY}} \boldsymbol{x}_i + \boldsymbol{t}_{\mathcal{XY}} - \boldsymbol{y}_{m(x_i)}\|^2. \tag{1}$$

Here, the rigid transformation is defined by a pair $[\boldsymbol{R}_{\mathcal{XY}}, \boldsymbol{t}_{\mathcal{XY}}]$, where $\boldsymbol{R}_{\mathcal{XY}} \in \mathrm{SO}(3)$ and $\boldsymbol{t}_{\mathcal{XY}} \in \mathbb{R}^3$; m maps from points in $\mathcal{X}$ to points in $\mathcal{Y}$. Assuming m is fixed, the alignment in (1) is given in closed-form by

$$\boldsymbol{R}_{\mathcal{XY}} = \boldsymbol{V} \boldsymbol{U}^\top \qquad \text{and} \qquad \boldsymbol{t}_{\mathcal{XY}} = -\boldsymbol{R}_{\mathcal{XY}} \overline{\boldsymbol{x}} + \overline{\boldsymbol{y}}, \tag{2}$$

where $\boldsymbol{U}$ and $\boldsymbol{V}$ are obtained using the singular value decomposition (SVD) $\boldsymbol{H} = \boldsymbol{U} \boldsymbol{S} \boldsymbol{V}^\top$, with $\boldsymbol{H} = \sum_{i=1}^{N} (\boldsymbol{x}_i - \overline{\boldsymbol{x}})(\boldsymbol{y}_{m(x_i)} - \overline{\boldsymbol{y}})^\top$. In this expression, centroids of $\mathcal{X}$ and $\mathcal{Y}$ are defined as $\overline{\boldsymbol{x}} = \frac{1}{N} \sum_{i=1}^{N} \boldsymbol{x}_i$ and $\overline{\boldsymbol{y}} = \frac{1}{N} \sum_{i=1}^{N} \boldsymbol{y}_{m(x_i)}$, respectively.

We can understand ICP and the more recent learning-based DCP method [2] as providing different choices of m:

Iterative Closest Point. ICP chooses m to minimize (1) with $[\boldsymbol{R}_{\mathcal{XY}}, \boldsymbol{t}_{\mathcal{XY}}]$ fixed, yielding:

$$m(\boldsymbol{x}_i, \mathcal{Y}) = \arg\min_{j} \|\boldsymbol{R}_{\mathcal{XY}} \boldsymbol{x}_i + \boldsymbol{t}_{\mathcal{XY}} - \boldsymbol{y}_j\|_2 \tag{3}$$

ICP approaches a fixed point by alternating between (2) and (3); each step decreases the objective (1). Since (1) is non-convex, however, there is no guarantee that ICP reaches a global optimum.

Deep Closest Point. DCP uses deep networks to learn m. In this method, $\mathcal{X}$ and $\mathcal{Y}$ are embedded using learned functions $\mathcal{F}_\mathcal{X}$ and $\mathcal{F}_\mathcal{Y}$ defined by a Siamese DGCNN [22]; these lifted point clouds are optionally contextualized by a Transformer module [59], yielding embeddings $\Phi_\mathcal{X}$ and $\Phi_\mathcal{Y}$. The mapping m is then

$$m(\boldsymbol{x}_i, \mathcal{Y}) = \mathrm{softmax}(\Phi_\mathcal{Y}\Phi_{\boldsymbol{x}_i}^\top). \tag{4}$$

This formula is applied in one shot followed by (2) to obtain the rigid alignment. The loss used to train this pipeline is mean-squared error (MSE) between ground-truth rigid motion from synthetically-rotated point clouds and prediction; the network is trained end-to-end.

3.2 Partial Registration Network

DCP is a one-shot algorithm, in that a single pass through the network determines the output for each prediction task. Analogously to ICP, PRNet is designed to be *iterative*; multiple passes of a point cloud through PRNet refine the alignment. The steps of PRNet, illustrated in Figure 1, are as follows:

1. take as input point clouds $\mathcal{X}$ and $\mathcal{Y}$;
2. detect keypoints of $\mathcal{X}$ and $\mathcal{Y}$;
3. predict a mapping from keypoints of $\mathcal{X}$ to keypoints of $\mathcal{Y}$;
4. predict a rigid transformation $[\boldsymbol{R}_{\mathcal{X}\mathcal{Y}}, \boldsymbol{t}_{\mathcal{X}\mathcal{Y}}]$ aligning $\mathcal{X}$ to $\mathcal{Y}$ based on the keypoints and map;
5. transform $\mathcal{X}$ using the obtained transformation;
6. return to 1 using the pair $(\boldsymbol{R}_{\mathcal{X}\mathcal{Y}}\mathcal{X} + \boldsymbol{t}_{\mathcal{X}\mathcal{Y}}, \mathcal{Y})$ as input.

When predicting a mapping from keypoints in $\mathcal{X}$ to keypoints in $\mathcal{Y}$, PRNet uses Gumbel–Softmax [3] to sample a matching matrix, which is sharper than (4) and approximately differentiable. It has a value network to predict a temperature for Gumbel–Softmax, so that the whole framework can be seen as an actor-critic method. We present details of and justifications behind the design below.

Notation. Denote by $\mathcal{X}^p = \{\boldsymbol{x}_1^p, \ldots, \boldsymbol{x}_i^p, \ldots, \boldsymbol{x}_N^p\}$ the rigid motion of $\mathcal{X}$ to align to $\mathcal{Y}$ after p applications of PRNet; $\mathcal{X}^1$ and $\mathcal{Y}^1$ are initial input shapes. We will use $[\boldsymbol{R}_{\mathcal{X}\mathcal{Y}}^p, \boldsymbol{t}_{\mathcal{X}\mathcal{Y}}^p]$ to denote the p-th rigid motion predicted by PRNet for the input pair $(\mathcal{X}, \mathcal{Y})$.

Since our training pairs are synthetically generated, before applying PRNet we know the ground-truth $[\boldsymbol{R}_{\mathcal{X}\mathcal{Y}}^*, \boldsymbol{t}_{\mathcal{X}\mathcal{Y}}^*]$ aligning $\mathcal{X}$ to $\mathcal{Y}$. From these values, during training we can compute "local" ground-truth $[\boldsymbol{R}_{\mathcal{X}\mathcal{Y}}^{p*}, \boldsymbol{t}_{\mathcal{X}\mathcal{Y}}^{p*}]$ on-the-fly, which maps the current $(\mathcal{X}^p, \mathcal{Y})$ to the best alignment:

$$\boldsymbol{R}_{\mathcal{X}\mathcal{Y}}^{p*} = \boldsymbol{R}_{\mathcal{X}\mathcal{Y}}^* \boldsymbol{R}_{\mathcal{X}\mathcal{Y}}^{1\ldots p\top} \quad \text{and} \quad \boldsymbol{t}_{\mathcal{X}\mathcal{Y}}^{p*} = \boldsymbol{t}_{\mathcal{X}\mathcal{Y}}^* - \boldsymbol{R}_{\mathcal{X}\mathcal{Y}}^{p*}\boldsymbol{t}_{\mathcal{X}\mathcal{Y}}^{1\ldots p}, \tag{5}$$

where

$$\boldsymbol{R}_{\mathcal{X}\mathcal{Y}}^{1\ldots p} = \boldsymbol{R}_{\mathcal{X}\mathcal{Y}}^{p-1} \ldots \boldsymbol{R}_{\mathcal{X}\mathcal{Y}}^1 \quad \text{and} \quad \boldsymbol{t}_{\mathcal{X}\mathcal{Y}}^{1\ldots p} = \boldsymbol{R}_{\mathcal{X}\mathcal{Y}}^{p-1}\boldsymbol{t}_{\mathcal{X}\mathcal{Y}}^{1\ldots p-1} + \boldsymbol{t}_{\mathcal{X}\mathcal{Y}}^{p-1}. \tag{6}$$

We use m^p to denote the mapping function in p-th step.

Synthesizing the notation above, $\mathcal{X}^p$ is given by

$$\boldsymbol{x}_i^p = \boldsymbol{R}_{\mathcal{X}\mathcal{Y}}^{p-1}\boldsymbol{x}_i^{p-1} + \boldsymbol{t}_{\mathcal{X}\mathcal{Y}}^{p-1} \tag{7}$$

where

$$\boldsymbol{R}_{\mathcal{X}\mathcal{Y}}^p = \boldsymbol{V}^p\boldsymbol{U}^{p\top} \quad \text{and} \quad \boldsymbol{t}_{\mathcal{X}\mathcal{Y}}^p = -\boldsymbol{R}_{\mathcal{X}\mathcal{Y}}^p\overline{\boldsymbol{x}}^p + \overline{\boldsymbol{y}}. \tag{8}$$

In this equation, $\boldsymbol{U}^p$ and $\boldsymbol{V}^p$ are computed using (2) from $\mathcal{X}^p$, $\mathcal{Y}^p$, and m^p.

Keypoint Detection. For partial-to-partial registration, usually $N \neq M$ and only subsets of $\mathcal{X}$ and $\mathcal{Y}$ match to one another. To detect these mutually-shared patches, we design a simple yet efficient keypoint detection module based on the observation that the L^2 norms of features tend to indicate whether a point is important.

Using $\mathcal{X}_k^p$ and $\mathcal{Y}_k^p$ to denote the k keypoints for $\mathcal{X}^p$ and $\mathcal{Y}^p$, we take

$$\mathcal{X}_k^p = \mathcal{X}^p(\mathrm{topk}(\|\Phi_{\boldsymbol{x}_1}^p\|_2, \ldots, \|\Phi_{\boldsymbol{x}_i}^p\|_2, \ldots, \|\Phi_{\boldsymbol{x}_N}^p\|_2)) \\ \mathcal{Y}_k^p = \mathcal{Y}^p(\mathrm{topk}(\|\Phi_{\boldsymbol{y}_1}^p\|_2, \ldots, \|\Phi_{\boldsymbol{y}_i}^p\|_2, \ldots, \|\Phi_{\boldsymbol{y}_M}^p\|_2)) \tag{9}$$

where $\mathrm{topk}(\cdot)$ extracts the indices of the k largest elements of the given input. Here, Φ denotes embeddings learned by DGCNN and Transformer.

By aligning only the keypoints, we remove irrelevant points from the two input clouds that are not shared in the partial correspondence. In particular, we can now solve the Procrustes problem that matches keypoints of $\mathcal{X}$ and $\mathcal{Y}$. We show in §4.3 that although we do not provide explicit supervision, PRNet still learns how to detect keypoints reasonably.

Gumbel–Softmax Sampler. One key observation in ICP and DCP is that (3) usually is not differentiable with respect to the map m but by definition yields a sharp correspondence between the points in $\mathcal{X}$ and the points in $\mathcal{Y}$. In contrast, the smooth function (4) in DCP is differentiable, but in exchange for this differentiability the mapping is blurred. We desire the best of both worlds: A potentially sharp mapping function that admits backpropagation.

To that end, we use Gumbel–Softmax [3] to sample a matching matrix. Using a straight-through gradient estimator, this module is approximately differentiable. In particular, the Gumbel–Softmax mapping function is given by

$$m^p(\boldsymbol{x}_i, \mathcal{Y}) = \mathrm{one\,hot}\left[\arg\max_j \mathrm{softmax}(\Phi^p_{\mathcal{Y}} \Phi^{p\top}_{\boldsymbol{x}_i} + g_{ij})\right], \tag{10}$$

where $(g_{i1}, \ldots, g_{ij}, \ldots, g_{iN})$ are i.i.d. samples drawn from Gumbel(0, 1). The map in (10) is not differentiable due to the discontinuity of $\arg\max$, but the straight-through gradient estimator [60] yields (biased) subgradient estimates with low variance. Following their methodology, on backward evaluation of the computational graph, we use (4) to compute $\frac{\partial L}{\partial \Phi^p_*}$, ignoring the $\mathrm{one\,hot}$ operator and the $\arg\max$ term.

Actor-Critic Closest Point (ACP). The mapping functions (4) and (10) have fixed "temperatures," that is, there is no control over the sharpness of the mapping matrix m^p. In PRNet, we wish to adapt the sharpness of the map based on the alignment of the two shapes. In particular, for low values of p (the initial iterations of alignment) we may satisfied with high-entropy approximate matchings that obtain a coarse alignment; later during iterative evaluations, we can sharpen the map to align individual pairs of points.

To make this intuition compatible with PRNet's learning-based architecture, we add a parameter λ to (10) to yield a generalized Gumbel–Softmax matching matrix:

$$m^p(\boldsymbol{x}_i, \mathcal{Y}) = \mathrm{one\,hot}\left[\arg\max_j \mathrm{softmax}\left(\frac{\Phi^p_{\mathcal{Y}} \Phi^{p\top}_{\boldsymbol{x}_i} + g_{ij}}{\lambda}\right)\right] \tag{11}$$

When λ is large, the map matrix m^p is smoothed out; as $\lambda \to 0$ the map approaches a binary matrix.

It is difficult to choose a single λ that suffices for all $(\mathcal{X}, \mathcal{Y})$ pairs; rather, we wish λ to be chosen adaptively and automatically to extract the best alignment for each pair of point clouds. Hence, we use a small network Θ to predict λ based on global features $\Psi^p_{\mathcal{X}}$ and $\Psi^p_{\mathcal{Y}}$ aggregated from $\Phi^p_{\mathcal{X}}$ and $\Phi^p_{\mathcal{Y}}$ channel-wise by global pooling (averaging). In particular, we take $\lambda = \Theta(\Psi^p_{\mathcal{X}}, \Psi^p_{\mathcal{Y}})$, where $\Psi^p_{\mathcal{X}} = \mathrm{avg}_i \Phi^p_{\boldsymbol{x}_i}$ and $\Psi^p_{\mathcal{Y}} = \mathrm{avg}_i \Phi^p_{\boldsymbol{y}_i}$. In the parlance of reinforcement learning, this choice can be seen as a simplified version of actor-critic method. $\Phi^p_{\mathcal{X}}$ and $\Phi^p_{\mathcal{Y}}$ are learned jointly with DGCNN [22] and Transformer [59]; then an actor head outputs a rigid motion, where (11) uses the λ predicted from a critic head.

Loss Function. The final loss L is the summation of several terms L_p, indexed by the number p of passes through PRNet for the input pair. L_p consists of three terms: a rigid motion loss L^m_p, a cycle consistency loss L^c_p, and a global feature alignment loss L_g. We also introduce a discount factor $\gamma < 1$ to promote alignment within the first few passes through PRNet; during training we pass each input pair through PRNet P times.

Combining the terms above, we have

$$L = \sum_{p=1}^{P} \gamma^{p-1} L_p, \qquad \text{where} \qquad L_p = L^m_p + \alpha L^c_p + \beta L^p_g. \tag{12}$$

The rigid motion loss L^m_p is,

$$L^m_p = \|\boldsymbol{R}^{p\top}_{\mathcal{X}\mathcal{Y}} \boldsymbol{R}^{p*}_{\mathcal{X}\mathcal{Y}} - I\|^2 + \|\boldsymbol{t}^p_{\mathcal{X}\mathcal{Y}} - \boldsymbol{t}^{p*}_{\mathcal{X}\mathcal{Y}}\|^2 \tag{13}$$

Model	MSE($\boldsymbol{R}$)↓	RMSE($\boldsymbol{R}$)↓	MAE($\boldsymbol{R}$)↓	R²($\boldsymbol{R}$)↑	MSE($\boldsymbol{t}$)↓	RMSE($\boldsymbol{t}$)↓	MAE($\boldsymbol{t}$)↓	R²($\boldsymbol{t}$)↑
ICP	1134.552	33.683	25.045	-5.696	0.0856	0.293	0.250	-0.037
Go-ICP [14]	195.985	13.999	3.165	-0.157	0.0011	0.033	0.012	0.987
FGR [61]	126.288	11.238	2.832	0.256	0.0009	0.030	0.008	0.989
PointNetLK [1]	280.044	16.735	7.550	-0.654	0.0020	0.045	0.025	0.975
DCP-v2 [2]	45.005	6.709	4.448	0.732	0.0007	0.027	0.020	0.991
PRNet (Ours)	**10.235**	**3.199257**	**1.454**	**0.939**	**0.0003**	**0.016**	**0.010**	**0.997**

Table 1: Test on unseen point clouds

Model	MSE($\boldsymbol{R}$)↓	RMSE($\boldsymbol{R}$)↓	MAE($\boldsymbol{R}$)↓	R²($\boldsymbol{R}$)↑	MSE($\boldsymbol{t}$)↓	RMSE($\boldsymbol{t}$)↓	MAE($\boldsymbol{t}$)↓	R²($\boldsymbol{t}$)↑
ICP	1217.618	34.894	25.455	-6.253	0.086	0.293	0.251	-0.038
Go-ICP [14]	157.072	12.533	2.940	0.063	0.0009	0.031	0.010	0.989
FGR [61]	98.635	9.932	**1.952**	0.414	0.0014	0.038	0.007	0.983
PointNetLK [1]	526.401	22.943	9.655	-2.137	0.0037	0.061	0.033	0.955
DCP-v2 [2]	95.431	9.769	6.954	0.427	0.0010	0.034	0.025	0.986
PRNet (Ours)	**24.857**	**4.986**	2.329	**0.850**	**0.0004**	**0.021**	**0.015**	**0.995**
PRNet (Ours*)	**15.624**	**3.953**	1.712	**0.907**	**0.0003**	**0.017**	**0.011**	**0.996**

Table 2: Test on unseen categories. PRNet (Ours*) denotes the model trained on ShapeNetCore and tested on ModelNet40 held-out categories. Others are trained on first 20 ModelNet40 categories and tested on ModelNet40 held-out categories.

Equation (5) gives the "localized" ground truth values for $\boldsymbol{R}^{p*}_{\mathcal{XY}}, \boldsymbol{t}^{p*}_{\mathcal{XY}}$. Denoting the rigid motion from $\mathcal{Y}$ to $\mathcal{X}$ in step p as $[\boldsymbol{R}^p_{\mathcal{YX}}, \boldsymbol{t}^p_{\mathcal{YX}}]$, the cycle consistency loss is

$$L^c_p = \|\boldsymbol{R}^p_{\mathcal{XY}}\boldsymbol{R}^p_{\mathcal{YX}} - I\|^2 + \|\boldsymbol{t}^p_{\mathcal{XY}} - \boldsymbol{t}^p_{\mathcal{YX}}\|^2. \tag{14}$$

Our last loss term is a global feature alignment loss, which enforces alignment of global features $\Psi^p_{\mathcal{X}}$ and $\Psi^p_{\mathcal{Y}}$. Mathematically, the global feature alignment loss is

$$L^p_g = \|\Psi^p_{\mathcal{X}} - \Psi^p_{\mathcal{Y}}\|. \tag{15}$$

This global feature alignment loss also provides signal for determining λ. When two shapes are close in global feature space, λ should be small, yielding a sharp matching matrix; when two shapes are far from each other, λ increases and the map is blurry.

4 Experiments

Our experiments are divided into four parts. First, we show performance of PRNet on a partial-to-partial registration task on synthetic data in §4.1. Then, we show PRNet can generalize to real data in §4.2. Third, we visualize the keypoints and correspondences predicted by PRNet in §4.3. Finally, we show a linear SVM trained on representations learned by PRNet can achieve comparable results to supervised learning methods in §4.4.

4.1 Partial-to-Partial Registration on ModelNet40

We evaluate partial-to-partial registration on ModelNet40 [62]. There are 12,311 CAD models spanning 40 object categories, split to 9,843 for training and 2,468 for testing. Point clouds are sampled from the CAD models by farthest-point sampling on the surface. During training, a point cloud with 1024 points $\mathcal{X}$ is sampled. Along each axis, we randomly draw a rigid transformation; the rotation along each axis is sampled in $[0, 45°]$ and translation is in $[-0.5, 0.5]$. We apply the rigid transformation to $\mathcal{X}$, leading to $\mathcal{Y}$. We simulate partial scans of $\mathcal{X}$ and $\mathcal{Y}$ by randomly placing a point in space and computing its 768 nearest neighbors in $\mathcal{X}$ and $\mathcal{Y}$ respectively.

We measure mean squared error (MSE), root mean squared error (RMSE), mean absolute error (MAE), and coefficient of determination (R²). Angular measurements are in units of degrees. MSE, RMSE and MAE should be zero while R² should be one if the rigid alignment is perfect. We compare our model to ICP, Go-ICP [14], Fast Global Registration (FGR) [61], and DCP [2].

Model	MSE($\boldsymbol{R}$)↓	RMSE($\boldsymbol{R}$)↓	MAE($\boldsymbol{R}$)↓	R²($\boldsymbol{R}$)↑	MSE($\boldsymbol{t}$)↓	RMSE($\boldsymbol{t}$)↓	MAE($\boldsymbol{t}$)↓	R²($\boldsymbol{t}$)↑
ICP	1229.670	35.067	25.564	-6.252	0.0860	0.294	0.250	-0.045
Go-ICP [14]	150.320	12.261	2.845	0.112	0.0008	0.028	0.029	0.991
FGR [61]	764.671	27.653	13.794	-3.491	0.0048	0.070	0.039	0.941
PointNetLK [1]	397.575	19.939	9.076	-1.343	0.0032	0.0572	0.032	0.960
DCP-v2 [2]	47.378	6.883	4.534	0.718	0.0008	0.028	0.021	0.991
PRNet (Ours)	**18.691**	**4.323**	**2.051**	**0.889**	**0.0003**	**0.017**	**0.012**	**0.995**

Table 3: Test on unseen point clouds with Gaussian noise

Figure 1 shows the architecture of ACP. We use DGCNN with 5 dynamic *EdgeConv* layers and a Transformer to learn co-contextual representations of $\mathcal{X}$ and $\mathcal{Y}$. The number of filters in each layer of DGCNN are $(64, 64, 128, 256, 512)$. In the Transformer, only one encoder and one decoder with 4-head attention are used. The embedding dimension is 1024. We train the network for 100 epochs using Adam [63]. The initial learning rate is 0.001 and is divided by 10 at epochs 30, 60, and 80.

Model	z/z ↑	SO(3)/SO(3) ↑	input size
PointNet [20]	89.2	83.6	2048×3
PointNet++ [21]	89.3	85.0	1024×3
DGCNN [22]	92.2	87.2	1024×3
VoxNet [64]	83.0	73.0	30^3
SubVolSup [65]	88.5	82.7	30^3
SubVolSup MO [65]	89.5	85.0	20×30^3
MVCNN 12x [66]	89.5	77.6	12×224^2
MVCNN 80x [66]	90.2	86.0	80×224^2
RotationNet 20x [67]	**92.4**	80.0	20×224^2
Spherical CNNs [68]	88.9	**86.9**	2×64^2
PRNet (Ours)	**85.2**	**80.5**	1024×3

Table 4: ModelNet40: transfer learning

Partial-to-Partial Registration on Unseen Objects. We first evaluate on the ModelNet40 train/test split. We train on 9,843 training objects and test on 2,468 testing objects. Table 1 shows performance. Our method outperforms its counterparts in all metrics.

Partial-to-Partial Registration on Unseen Categories. We follow the same testing protocol as [2] to compare the generalizability of different models. ModelNet40 is split evenly by category into training and testing sets. PRNet and DCP are trained on the first 20 categories, and then all methods are tested on the held-out categories. Table 2 shows PRNet behaves more strongly than others. To further test generalizability, we train it on ShapeNetCore dataset [69] and test on ModelNet40 held-out categories. ShapeNetCore has 57,448 objects, and we do the same preprocessing as on ModelNet40. The last row in Table 2, denoted as PRNet (Ours*), surprisingly shows PRNet performs much better than when trained on ModelNet40. This supports the intuition that data-driven approaches work better with more data.

Partial-to-Partial Registration on Unseen Objects with Gaussian Noise. We further test robustness to noise. The same preprocessing is done as in the first experiment, except that noise independently sampled from $\mathcal{N}(0, 0.01)$ and clipped to $[-0.05, 0.05]$ is added to each point. As in Table 3, learning-based methods, including DCP and PRNet, are more robust. In particular, PRNet exhibits stronger performance and is even comparable to the noise-free version in Table 1.

4.2 Partial-to-Partial on Real Data

We test our model on the Stanford Bunny dataset [70]. Since the dataset only has 10 real scans, we fine tune the model used in Table 1 for 10 epochs with learning rate 0.0001. For each scan, we generate 100 training examples by randomly transforming the scan in the same way as we do in §4.1. This training procedure can be viewed as inference time fine-tuning, in contrast to optimization-based methods that perform one-time inference for each test case. Figure 2 shows the results. We further test our model on more scans from Stanford 3D Scanning Repository [71] using a similar methodology; Figure 3 shows the registration results.
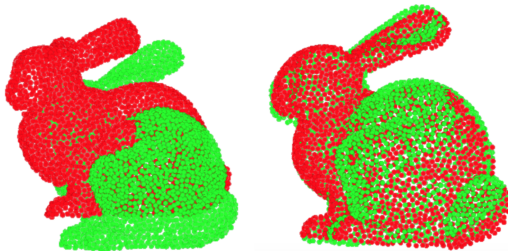

Figure 2: Left: Input partial point clouds. Right: Transformed partial point clouds.
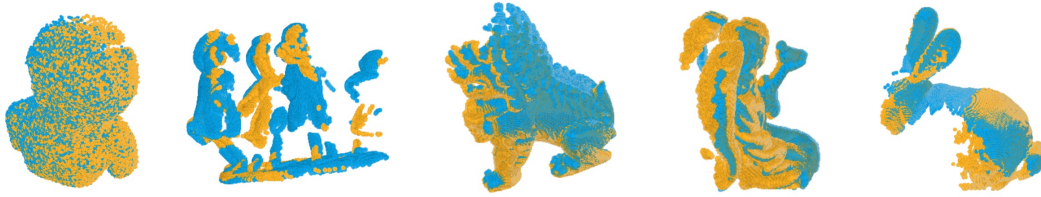
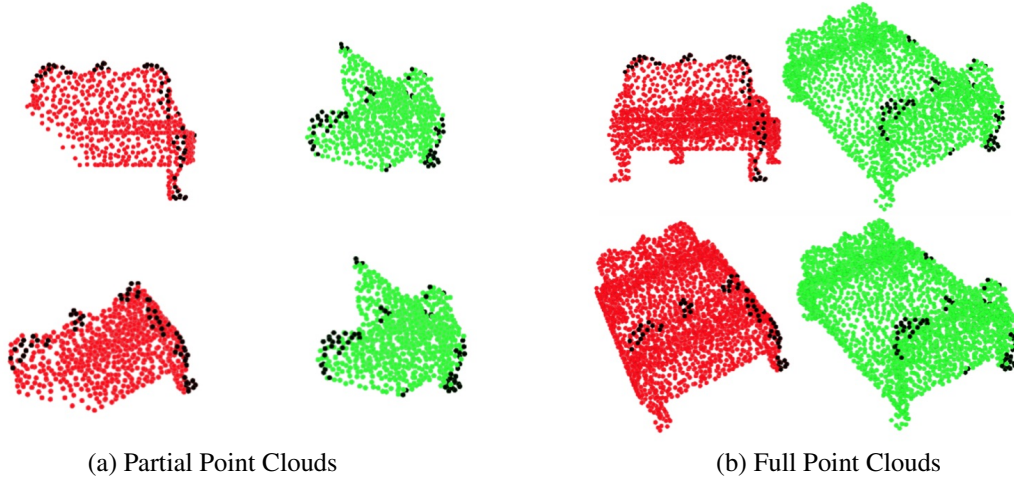Figure 3: More examples on The Stanford 3D Scanning Repository [71].

(a) Partial Point Clouds (b) Full Point Clouds

Figure 4: Keypoint detection of a pair of beds. Point clouds in red are $\mathcal{X}$ and point clouds in green are $\mathcal{Y}$. Points in black are keypoints detected by PRNet. Point clouds in the first row are in the original pose while point clouds in the second row are transformed using the rigid transformation predicted by PRNet. (a) PRNet takes as input partial point clouds. (b) The obtained rigid transformation is applied to full point clouds for better visualization.
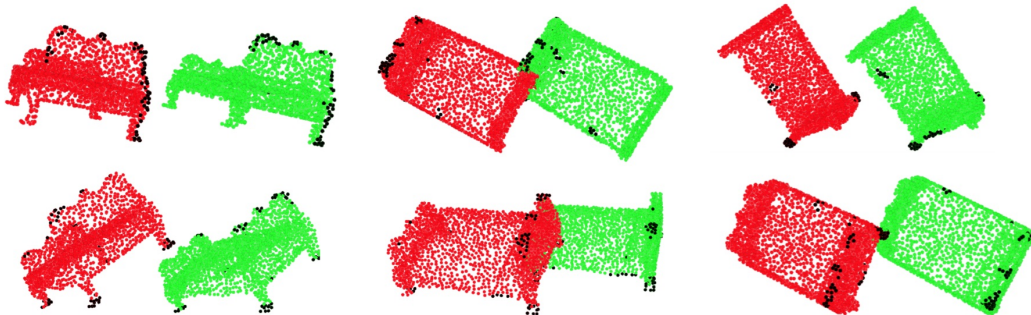
Figure 5: Keypoint detection with different partial scans. We show the same pair of $\mathcal{X}$ and $\mathcal{Y}$ with different views. The keypoints are data-dependent and consistent across different views.

4.3 Keypoints and Correspondences

We visualize keypoints on several objects in Figure 4 and correspondences in Figure 6. The model detects keypoints and correspondences on partially observable objects. We overlay the keypoints on top of the fully observable objects. Also, as shown in Figure 5, the keypoints are consistent across different views.
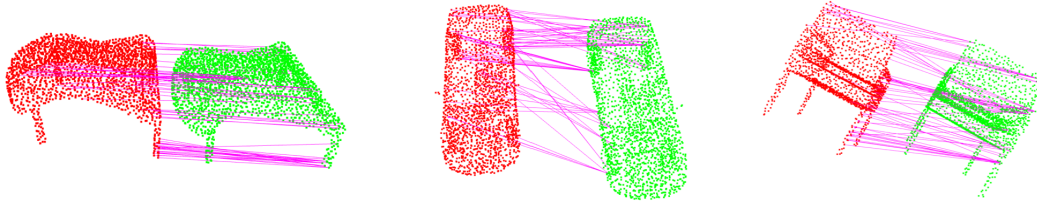
Figure 6: Correspondences for pairs of objects.

4.4 Transfer to Classification

Representations learned by PRNet can be transferred to object recognition. We use the model trained on ShapeNetCore in §4.1 and train a linear SVM on top of the embeddings predicted by DGCNN. In Table 4, we show classification accuracy on ModelNet40. z/z means the model is trained when only azimuthal rotations are present on both during and testing. $SO(3)/SO(3)$ means the object is moved with a random motion in $SO(3)$ during both training and testing. Although other methods are supervised, ours achieves comparable performance.

5 Conclusion

PRNet tackles a general partial-to-partial registration problem, leveraging self-supervised learning to learn geometric priors directly from data. The success of PRNet verifies the sensibility of applying learning to partial matching as well as the specific choice of Gumbel–Softmax, which we hope can inspire additional work linking discrete optimization to deep learning. PRNet is also a reinforcement learning-like framework; this connection between registration and reinforcement learning may provide inspiration for additional interdisciplinary research related to rigid/non-rigid registration.

Our experiments suggest several avenues for future work. For example, as shown in Figure 6, the matchings computed by PRNet are not bijective, evident e.g. in the point clouds of cars and chairs. One possible extension of our work to address this issue is to use Gumbel–Sinkhorn [72] to encourage bijectivity. Improving the efficiency of PRNet when applied to real scans also will be extremely valuable. As described in §4.2, PRNet currently requires inference-time fine-tuning on real scans to learn useful data-dependent representations; this makes PRNet slow during inference. Seeking universal representations that generalize over broader sets of registration tasks will improve the speed and generalizability of learning-based registration. Another possibility for future work is to improve the scalability of PRNet to deal with large-scale real scans captured by LiDAR.

Finally, we hope to find more applications of PRNet beyond the use cases we have shown in the paper. A key direction bridging PRNet to applications will involve incorporating our method into SLAM or structure-from-motion can demonstrate its value for robotics applications and robustness to realistic species of noise. Additionally, we can test the effectiveness of PRNet for registration problems in medical imaging and/or high-energy particle physics.

6 Acknowledgements

References

[1] Hunter Goforth, Yasuhiro Aoki, R. Arun Srivatsan, and Simon Lucey. PointNetLK: Robust & efficient point cloud registration using PointNet. In *IEEE Conference on Computer Vision and Pattern Recognition*

(CVPR), 2019.

[2] Yue Wang and Justin Solomon. Deep closest point: Learning representations for point cloud registration. In *IEEE International Conference on Computer Vision (ICCV)*, 2019.

[3] Eric Jang, Shixiang Gu, and Ben Poole. Categorical reparameterization with Gumbel-Softmax. In *International Conference on Learning Representations (ICLR)*, 2017.

[4] Chengzhou Tang and Ping Tan. BA-net: Dense bundle adjustment networks. In *International Conference on Learning Representations (ICLR)*, 2019.

[5] Paul J. Besl and Neil D. McKay. A method for registration of 3-d shapes. *IEEE Transactions on Pattern Analysis and Machine Intelligence (PAMI)*, 14(2):239–256, February 1992.

[6] Szymon Rusinkiewicz and Marc Levoy. Efficient variants of the ICP algorithm. In *Third International Conference on 3D Digital Imaging and Modeling (3DIM)*, 2001.

[7] Aleksandr Segal, Dirk Hähnel, and Sebastian Thrun. Generalized-ICP. In *Robotics: Science and Systems*, 2009.

[8] Sofien Bouaziz, Andrea Tagliasacchi, and Mark Pauly. Sparse iterative closest point. In *Proceedings of the Symposium on Geometry Processing*, 2013.

[9] François Pomerleau, Francis Colas, and Roland Siegwart. A review of point cloud registration algorithms for mobile robotics. *Now Foundations and Trends*, 4(1):1–104, May 2015.

[10] Gabriel Agamennoni, Simone Fontana, Roland Y. Siegwart, and Domenico G. Sorrenti. Point clouds registration with probabilistic data association. In *International Conference on Intelligent Robots and Systems (IROS)*, 2016.

[11] Timo Hinzmann, Thomas Stastny, Gianpaolo Conte, Patrick Doherty, Piotr Rudol, Marius Wzorek, Enric Galceran, Roland Siegwart, and Igor Gilitschenski. Collaborative 3d reconstruction using heterogeneous UAVs: System and experiments. In *International Symposium on Robotic Research*, 2016.

[12] Dirk Hähnel and Wolfram Burgard. Probabilistic matching for 3d scan registration. In *Proceedings of the VDI - Conference Robotik (Robotik)*, 2002.

[13] Andrew W. Fitzgibbon. Robust registration of 2D and 3D point sets. In *British Machine Vision Conference (BMVC)*, 2001.

[14] Jiaolong Yang, Hongdong Li, Dylan Campbell, and Yunde Jia. Go-ICP: A globally optimal solution to 3d ICP point-set registration. *IEEE Transactions on Pattern Analysis and Machine Intelligence (PAMI)*, 38(11):2241–2254, November 2016.

[15] David M. Rosen, Luca Carlone, Afonso S. Bandeira, and John J. Leonard. SE-Sync: A certifiably correct algorithm for synchronization over the Special Euclidean group. In *The Workshop on the Algorithmic Foundations of Robotics (WAFR)*, 2016.

[16] Haggai Maron, Nadav Dym, Itay Kezurer, Shahar Kovalsky, and Yaron Lipman. Point registration via efficient convex relaxation. *ACM Transactions on Graphics (TOG)*, 35(4):73:1–73:12, July 2016.

[17] Gregory Izatt, Hongkai Dai, and Russ Tedrake. Globally optimal object pose estimation in point clouds with mixed-integer programming. In *International Symposium on Robotic Research*, 2017.

[18] Heng Yang and Luca Carlone. A polynomial-time solution for robust registration with extreme outlier rates. In *Robotics: Science and Systems*, 2019.

[19] Manzil Zaheer, Satwik Kottur, Siamak Ravanbakhsh, Barnabas Poczos, Ruslan Salakhutdinov, and Alexander Smola. Deep sets. In *Advances in Neural Information Processing Systems*, 2017.

[20] Charles Ruizhongtai Qi, Hao Su, Kaichun Mo, and Leonidas J. Guibas. PointNet: Deep learning on point sets for 3d classification and segmentation. In *IEEE Conference on Computer Vision and Pattern Recognition (CVPR)*, 2017.

[21] Charles Ruizhongtai Qi, Li Yi, Hao Su, and Leonidas J Guibas. PointNet++: Deep hierarchical feature learning on point sets in a metric space. In *Advances in Neural Information Processing Systems*, 2017.

[22] Yue Wang, Yongbin Sun, Sanjay E. Sarma Ziwei Liu, Michael M. Bronstein, and Justin M. Solomon. Dynamic graph CNN for learning on point clouds. *ACM Transactions on Graphics (TOG)*, 38:146, 2019.

[23] Yangyan Li, Rui Bu, Mingchao Sun, Wei Wu, Xinhan Di, and Baoquan Chen. PointCNN: Convolution on X-transformed points. In *Advances in Neural Information Processing Systems*, 2018.

[24] Matan Atzmon, Haggai Maron, and Yaron Lipman. Point convolutional neural networks by extension operators. *ACM Transactions on Graphics (TOG)*, 37(4):71:1–71:12, July 2018.

[25] David K Duvenaud, Dougal Maclaurin, Jorge Iparraguirre, Rafael Bombarell, Timothy Hirzel, Alan Aspuru-Guzik, and Ryan P Adams. Convolutional networks on graphs for learning molecular fingerprints. In *Advances in Neural Information Processing Systems*, 2015.

[26] Thomas N Kipf and Max Welling. Semi-supervised classification with graph convolutional networks. In *International Conference on Learning Representations (ICLR)*, 2017.

[27] Federico Monti, Davide Boscaini, Jonathan Masci, Emanuele Rodolà, Jan Svoboda, and Michael M. Bronstein. Geometric deep learning on graphs and manifolds using mixture model cnns. In *IEEE Conference on Computer Vision and Pattern Recognition (CVPR)*, 2017.

[28] Yu Wang, Vladimir Kim, Michael Bronstein, and Justin Solomon. Learning geometric operators on meshes. *Representation Learning on Graphs and Manifolds (ICLR workshop)*, 2019.

[29] Michael M Bronstein, Joan Bruna, Yann LeCun, Arthur Szlam, and Pierre Vandergheynst. Geometric deep learning: going beyond Euclidean data. *IEEE Signal Processing Magazine*, 34(4):18–42, 2017.

[30] Hang Su, Varun Jampani, Deqing Sun, Subhransu Maji, Evangelos Kalogerakis, Ming-Hsuan Yang, and Jan Kautz. SPLATNet: Sparse lattice networks for point cloud processing. In *IEEE Conference on Computer Vision and Pattern Recognition (CVPR)*, 2018.

[31] Matthias Fey, Jan Eric Lenssen, Frank Weichert, and Heinrich Müller. SplineCNN: Fast geometric deep learning with continuous B-spline kernels. In *Computer Vision and Pattern Recognition (CVPR)*, 2018.

[32] Hugues Thomas, Charles Ruizhongtai Qi, Jean-Emmanuel Deschaud, Beatriz Marcotegui, Franccois Goulette, and Leonidas J. Guibas. KPConv: Flexible and deformable convolution for point clouds. In *International Conference on Computer Vision (ICCV)*, 2019.

[33] Danielle Ezuz, Justin Solomon, Vladimir G. Kim, and Mirela Ben-Chen. GWCNN: A metric alignment layer for deep shape analysis. *Computer Graphics Forum*, 2017.

[34] Alexander M Bronstein, Michael Bronstein, and Ron Kimmel. Generalized multidimensional scaling: A framework for isometry-invariant partial surface matching. In *Proceedings of the National Academy of Sciences of the United States of America*, 2006.

[35] Qi-Xing Huang, Bart Adams, Martin Wicke, and Leonidas J. Guibas. Non-rigid registration under isometric deformations. In *Proceedings of the Symposium on Geometry Processing*, 2008.

[36] Yaron Lipman and Thomas Funkhouser. Möbius voting for surface correspondence. In *ACM SIGGRAPH*, 2009.

[37] Vladimir G. Kim, Yaron Lipman, and Thomas Funkhouser. Blended intrinsic maps. In *ACM SIGGRAPH*, 2011.

[38] Justin Solomon, Andy Nguyen, Adrian Butscher, Mirela Ben-Chen, and Leonidas Guibas. Soft maps between surfaces. *Computer Graphics Forum*, 31(5):1617–1626, August 2012.

[39] Justin Solomon, Leonidas Guibas, and Adrian Butscher. Dirichlet energy for analysis and synthesis of soft maps. In *Proceedings of the Symposium on Geometry Processing*, 2013.

[40] Justin Solomon, Gabriel Peyré, Vladimir G. Kim, and Suvrit Sra. Entropic metric alignment for correspondence problems. *ACM Transactions on Graphics (TOG)*, 35(4):72:1–72:13, July 2016.

[41] Danielle Ezuz, Justin Solomon, and Mirela Ben-Chen. Reversible harmonic maps between discrete surfaces. *ACM Transactions on Graphics (TOG)*, 38(2):15:1–15:12, March 2019.

[42] Maks Ovsjanikov, Mirela Ben-Chen, Justin Solomon, Adrian Butscher, and Leonidas Guibas. Functional maps: A flexible representation of maps between shapes. *ACM Transactions on Graphics (TOG)*, 31(4):30:1–30:11, July 2012.

[43] Or Litany, Tal Remez, Emanuele Rodolà, Alex Bronstein, and Michael Bronstein. Deep functional maps: Structured prediction for dense shape correspondence. In *International Conference on Computer Vision (ICCV)*, 2017.

[44] Oshri Halimi, Or Litany, Emanuele Rodolà, Alex Bronstein, and Ron Kimmel. Self-supervised learning of dense shape correspondence. In *IEEE Conference on Computer Vision and Pattern Recognition (CVPR)*, 2019.

[45] Supasorn Suwajanakorn, Noah Snavely, Jonathan J Tompson, and Mohammad Norouzi. Discovery of latent 3d keypoints via end-to-end geometric reasoning. In *Advances in Neural Information Processing Systems (NeurIPS)*, 2018.

[46] Li Yi, Haibin Huang, Difan Liu, Evangelos Kalogerakis, Hao Su, and Leonidas Guibas. Deep part induction from articulated object pairs. *ACM Transactions on Graphics (TOG)*, 37(6):209:1–209:15, December 2018.

[47] Richard Zhang, Phillip Isola, and Alexei A Efros. Colorful image colorization. In *European Conference on Computer Vision (ECCV)*, 2016.

[48] Richard Zhang, Phillip Isola, and Alexei A Efros. Split-brain autoencoders: Unsupervised learning by cross-channel prediction. In *Computer Vision and Pattern Recognition (CVPR)*, 2017.

[49] Lluis Castrejon, Yusuf Aytar, Carl Vondrick, Hamed Pirsiavash, and Antonio Torralba. Learning aligned cross-modal representations from weakly aligned data. In *Computer Vision and Pattern Recognition (CVPR)*, 2016.

[50] Yusuf Aytar, Lluis Castrejon, Carl Vondrick, Hamed Pirsiavash, and Antonio Torralba. Cross-modal scene networks. *CoRR*, abs/1610.09003, 2016.

[51] Jacob Devlin, Ming-Wei Chang, Kenton Lee, and Kristina Toutanova. BERT: pre-training of deep bidirectional transformers for language understanding. In *The Annual Conference of the North American Chapter of the Association for Computational Linguistics (NAACL)*, 2018.

[52] Kaiming He, Ross B. Girshick, and Piotr Dollár. Rethinking imagenet pre-training. In *Computer Vision and Pattern Recognition (CVPR)*, 2019.

[53] Hang Zhao, Chuang Gan, Andrew Rouditchenko, Carl Vondrick, Josh McDermott, and Antonio Torralba. The sound of pixels. In *European Conference on Computer Vision (ECCV)*, 2018.

[54] Andrew Oweppns and Alexei A Efros. Audio-visual scene analysis with self-supervised multisensory features. In *European Conference on Computer Vision (ECCV)*, 2018.

[55] Ariel Ephrat, Inbar Mosseri, Oran Lang, Tali Dekel, Kevin Wilson, Avinatan Hassidim, William T. Freeman, and Michael Rubinstein. Looking to listen at the cocktail party: A speaker-independent audio-visual model for speech separation. *ACM Transactions on Graphics*, 37(4):112:1–112:11, July 2018.

[56] Volodymyr Mnih, Adria Puigdomenech Badia, Mehdi Mirza, Alex Graves, Timothy Lillicrap, Tim Harley, David Silver, and Koray Kavukcuoglu. Asynchronous methods for deep reinforcement learning. In *International Conference on Machine Learning (ICML)*, 2016.

[57] David Pfau and Oriol Vinyals. Connecting generative adversarial networks and actor-critic methods. In *NeurIPS Workshop on Adversarial Training*, 2016.

[58] Dzmitry Bahdanau, Philemon Brakel, Kelvin Xu, Anirudh Goyal, Ryan Lowe, Joelle Pineau, Aaron C. Courville, and Yoshua Bengio. An actor-critic algorithm for sequence prediction. In *International Conference on Learning Representations, ICLR*, 2017.

[59] Ashish Vaswani, Noam Shazeer, Niki Parmar, Jakob Uszkoreit, Llion Jones, Aidan N Gomez, Łukasz Kaiser, and Illia Polosukhin. Attention is all you need. In *Advances in Neural Information Processing Systems (NeurIPS)*, 2017.

[60] Yoshua Bengio. Estimating or propagating gradients through stochastic neurons. *CoRR*, abs/1305.2982, 2013.

[61] Qian-Yi Zhou, Jaesik Park, and Vladlen Koltun. Fast global registration. In *European Conference on Computer Vision (ECCV)*, 2016.

[62] Zhirong Wu, Shuran Song, Aditya Khosla, Linguang Zhang, Xiaoou Tang, and Jianxiong Xiao. 3d ShapeNets: A deep representation for volumetric shape modeling. In *IEEE Conference on Computer Vision and Pattern Recognition (CVPR)*, 2015.

[63] Diederik P. Kingma and Jimmy Ba. Adam: A method for stochastic optimization. In *International Conference for Learning Representations (ICLR)*, 2015.

[64] Daniel Maturana and Sebastian Scherer. Voxnet: A 3d convolutional neural network for real-time object recognition. In *International Conference on Intelligent Robots and Systems*, 2015.

[65] Charles Ruizhongtai Qi, Hao Su, Matthias Nießner, Angela Dai, Mengyuan Yan, and Leonidas Guibas. Volumetric and multi-view CNNs for object classification on 3d data. In *Computer Vision and Pattern Recognition (CVPR)*, 2016.

[66] Hang Su, Subhransu Maji, Evangelos Kalogerakis, and Erik G. Learned-Miller. Multi-view convolutional neural networks for 3d shape recognition. In *International Conference on Computer Vision (ICCV)*, 2015.

[67] Asako Kanezaki, Yasuyuki Matsushita, and Yoshifumi Nishida. RotationNet: Joint object categorization and pose estimation using multiviews from unsupervised viewpoints. In *Computer Vision and Pattern Recognition (CVPR)*, 2018.

[68] Carlos Esteves, Christine Allen-Blanchette, Ameesh Makadia, and Kostas Daniilidis. Learning SO(3) equivariant representations with spherical CNNs. In *European Conference on Computer Vision (ECCV)*, 2017.

[69] Angel Xuan Chang, Thomas A. Funkhouser, Leonidas J. Guibas, Pat Hanrahan, Qi-Xing Huang, Zimo Li, Silvio Savarese, Manolis Savva, Shuran Song, Hao Su, Jianxiong Xiao, Li Yi, and Fisher Yu. ShapeNet: An information-rich 3d model repository. *CoRR*, abs/1512.03012, 2015.

[70] Greg Turk and Marc Levoy. Zippered polygon meshes from range images. In *Proceedings of the 21st Annual Conference on Computer Graphics and Interactive Techniques*, 1994.

[71] The Stanford 3d scanning repository.

[72] Gonzalo Mena, David Belanger, Scott Linderman, and Jasper Snoek. Learning latent permutations with Gumbel–Sinkhorn networks. In *International Conference on Learning Representations (ICLR)*, 2018.

Model	MSE($\boldsymbol{R}$)↓	RMSE($\boldsymbol{R}$)↓	MAE($\boldsymbol{R}$)↓	R^2($\boldsymbol{R}$)↑	MSE($\boldsymbol{t}$)↓	RMSE($\boldsymbol{t}$)↓	MAE($\boldsymbol{t}$)↓	R^2($\boldsymbol{t}$)↑
Fixed λ	13.661	3.696	1.659	0.919	0.0003	0.018	0.012	0.996
Annealed λ	12.732	3.568	1.630	0.924	0.0003	0.017	0.011	0.996
Learned λ	13.506	3.675	1.675	0.920	0.0003	0.018	0.012	0.996
Predicted λ	**10.235**	**3.199257**	**1.454**	**0.939**	**0.0003**	**0.016**	**0.010**	**0.997**

Table 5: Choices of λ

Supplementary

We provide more details of PRNet in this section.

Actor-Critic Closest Point. A shared DGCNN [22] is to use extract embeddings for $\mathcal{X}$ and $\mathcal{Y}$ separately. The number of filters per layer are $(64, 64, 128, 256, 512)$. We use BatchNorm and LeakyReLU after each MLP in the EdgeConv layer. The local aggregation function of k-nn graph is max, and there is no global aggregation function used in DGCNN. $\mathcal{F}_{\mathcal{X}}$ and $\mathcal{F}_{\mathcal{Y}}$ denote the representations learned by DGCNN.

After DGCNN, $\mathcal{F}_{\mathcal{X}}$ and $\mathcal{F}_{\mathcal{Y}}$ are fed into the Transformer. The Transformer is an asymmetric function that learns co-contextual representations $\Phi_{\mathcal{X}}$ and $\Phi_{\mathcal{Y}}$. Transformer has only one encoder and one decoder. 4-head self-attention is used in encoder and decoder. LayerNorm, instead of BatchNorm, is used in the Transformer. Unlike the original implementation of Transformer, we do not use Dropout. For detailed presentation of Transformer, we refer readers to the tutorial.[2]

There are two heads on top of the representations $\Phi_{\mathcal{X}}$ and $\Phi_{\mathcal{Y}}$: a action head consisting of Gumbel-Softmax and SVD; a value head to predict a λ for Gumbel-Softmax in the action head. The value head is parameterized by a 4-layer MLPs. The number of filters are $(128, 128, 128, 1)$. BatchNorm and ReLU are used after each linear layer in the MLPs.

Training Protocol. We train the model for 100 epochs. At epochs 30, 60, and 80, we divide the learning rate by 10; it is initially 0.001. Each training pair $\mathcal{X}$ and $\mathcal{Y}$ is passed through PRNet three times iteratively (the rigid alignment of $\mathcal{X}$ is updated three times). The final rigid transformation is the combination of these three local rigid transformations. α for cycle consistency loss and β for feature alignment loss are both 0.1. The weight decay used is 10^{-4}. The number of keypoints is 512 on training. For visualization purposes, however, we show 64 keypoints in Figure 4, Figure 5, and Figure 6.

Our model is trained on a Google Cloud GPU instance with 4 Tesla V100 GPUs and takes 10 hours to complete.

As for DCP-v2, we take the implementation from the authors' released code [3] and train it as they suggest.

Choices of λ. We compare to alternative choices of ways to determine λ: (1) fixing λ manually; (2) annealing λ to near 0 as the training going; (3) including λ as a variable during training. We train the PRNet in the same way for each option, except the choice of λ is different. Table 5 verifies our choice of strategies for computing λ.

Keypoint detection alternatives, experiments on full point clouds, effects of discount factor, choice of k, robustness to data missing ratio, robustness to data noise. To understand the effectiveness of each part, we conduct additional experiments in Table 6; to save space, we only show MAE and R^2. (a) First, we consider alternatives to keypoint selection: in the first alternative, the two sets of keypoints are chosen independently and randomly on the two surfaces ($\mathcal{X}$ and $\mathcal{Y}$); in the second alternative, we use *centrality* to choose keypoints, keeping the k points whose average distance (in feature space) to the rest in the point cloud is minimal. Empirically, the L^2 norm used in our pipeline to select keypoints outperforms others. (b) Second, we compare our method to others on full point clouds. In this experiment, 768 points are sampled from each point cloud to cover the

---

[2]`http://nlp.seas.harvard.edu/2018/04/03/attention.html`
[3]`https://github.com/WangYueFt/dcp`

Method	MAE($\boldsymbol{R}$)↓	R^2($\boldsymbol{R}$)↑	MAE($\boldsymbol{t}$)↓	R^2($\boldsymbol{t}$)↑
Random sampling	1.689	0.927	0.011	**0.997**
Closeness to other points	2.109	0.861	0.013	0.995
L^2 Norm	**1.454**	**0.939**	**0.010**	0.997

(a) Different keypoint detection methods.

Model	MAE($\boldsymbol{R}$)↓	R^2($\boldsymbol{R}$)↑	MAE($\boldsymbol{t}$)↓	R^2($\boldsymbol{t}$)↑
ICP	25.165	-5.860	0.250	-0.045
Go-ICP	2.336	0.308	0.007	0.994
FGR	2.088	0.393	**0.003**	0.999
PointNetLK	3.478	0.051	0.005	0.994
DCP	2.777	0.887	0.009	0.998
PRNet (Ours)	**0.960**	**0.979**	0.006	**1.000**

(b) Experiments on full point clouds.

Discount Factor λ	MAE($\boldsymbol{R}$)↓	R^2($\boldsymbol{R}$)↑	MAE($\boldsymbol{t}$)↓	R^2($\boldsymbol{t}$)↑
0.5	1.921	0.917	0.014	0.995
0.7	1.998	0.884	0.014	0.995
0.9	**1.454**	**0.939**	**0.010**	**0.997**
0.99	1.732	0.915	0.012	0.996

(c) Different discount factors (λ).

Different k	MAE($\boldsymbol{R}$)↓	R^2($\boldsymbol{R}$)↑	MAE($\boldsymbol{t}$)↓	R^2($\boldsymbol{t}$)↑
16	27.843	-14.176	0.136	0.326
32	8.293	-1.848	0.048	0.892
64	3.129	0.563	0.024	0.979
128	2.007	0.879	0.016	0.991
256	1.601	0.932	0.012	0.996
384	1.508	0.934	0.011	**0.997**
512	**1.454**	**0.939**	**0.010**	**0.997**

(d) Different number of keypoints (k).

Data Missing Ratio	MAE($\boldsymbol{R}$)↓	R^2($\boldsymbol{R}$)↑	MAE($\boldsymbol{t}$)↓	R^2($\boldsymbol{t}$)↑
75%	6.447	0.028	0.042	0.921
50%	3.939	0.623	0.0288	0.969
25%	**1.454**	**0.939**	**0.010**	**0.997**

(e) Data missing ratio.

Data Noise	MAE($\boldsymbol{R}$)↓	R^2($\boldsymbol{R}$)↑	MAE($\boldsymbol{t}$)↓	R^2($\boldsymbol{t}$)↑
$\mathcal{N}(0, 0.01^2)$	**2.051**	**0.889**	**0.012**	**0.995**
$\mathcal{N}(0, 0.1^2)$	5.013	0.617	0.020	0.991
$\mathcal{N}(0, 0.5^2)$	21.129	-2.830	0.064	0.917

(f) Data noise.

Table 6: Ablation studies.

# points	ICP	Go-ICP	FGR	PointNetLK	DCP	PRNet
512	0.134	14.763	0.230	0.049	0.014	0.042
1024	0.170	14.853	0.250	0.061	0.024	0.073
2048	0.242	14.929	0.248	0.069	0.058	0.152

Table 7: Inference time (in seconds).

full shape using farthest-point sampling. In the full point cloud setting, PRNet still outperforms others. (c) Third, we verify our choice of discount factor λ; small large discount factors encourage alignment within the first few passes through PRNet while large discount factors promote longer-term return. (d) Fourth, we test the choice of number of keypoints: the model achieves surprisingly good performance even with 64 keypoints, but performance drops significantly when $k < 32$. (e) Fifth, we test its robustness to missing data. The missing data ratio in original partial-to-partial experiment is 25%; we further test with 50% and 75%. This test shows that with 75% points missing, the method still achieves reasonable performance, even compared to other methods tested with only 25% points missing. (f) Finally, we test the model robustness to noise level. Noise is sampled from $\mathcal{N}(0, \sigma^2)$. The model is trained with $\sigma = 0.01$ and tested with $\sigma \in [0.01, 0.1, 0.5]$. Even with $\sigma = 0.1$, the model still performs reasonably well.

Efficiency. We benchmark the inference time of different methods on a desktop computer with an Intel 16-core CPU, an Nvidia GTX 1080 Ti GPU, and 128G memory. Table 7 shows learning based methods (on GPUs) are faster than non-learning based counterparts (on CPUs). PRNet is on a par with PointNetLK while being slower than DCP.

More figures of keypoints and correspondences. In Figure 7 and Figure 8, we show more visualizations of keypoints and correspondences for different pairs of objects.
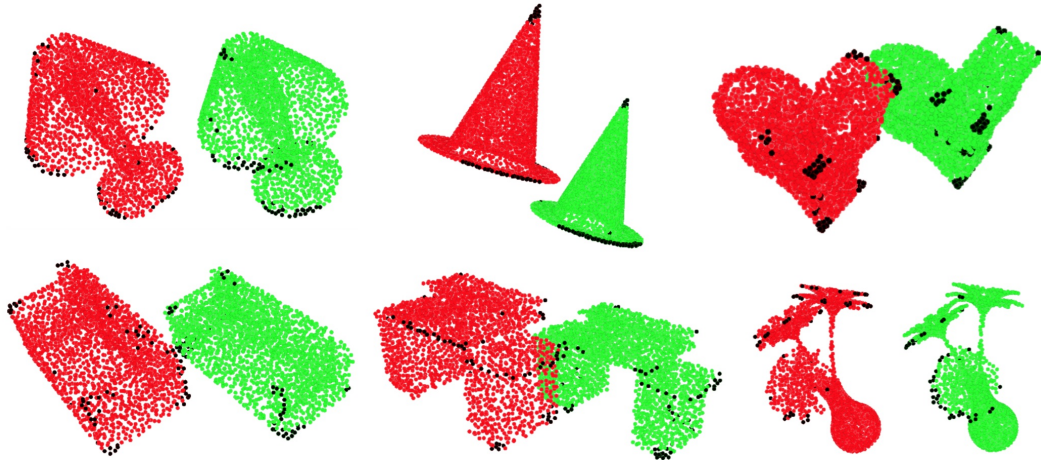
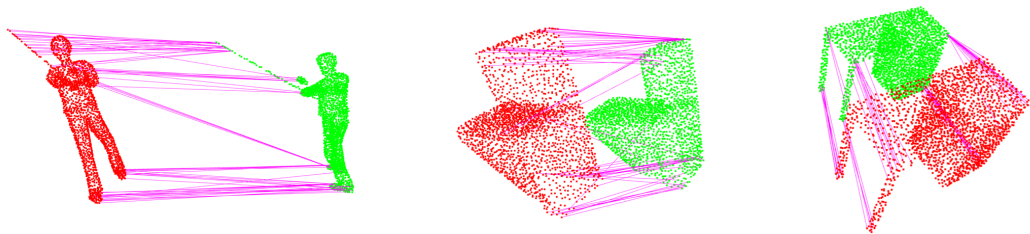Figure 7: Keypoint detection for different pairs of objects.

Figure 8: Correspondence prediction for different pairs of objects.